Understanding High-Speed Aeroelastic Stability of a Hingeless Hub Proprotor

Nathan T. O'Brien* and Anubhav Datta†
University of Maryland, College Park, Maryland 20742

https://doi.org/10.2514/1.C038655

A 4.75-ft-diameter dynamically scaled hingeless-hub proprotor model was developed and tested for aeroelastic stability up to 200 kt–corresponding to 468 kt full scale. The model had interchangeable hubs, blades, and pylon center-of-gravity locations, allowing data acquisition for new parametric variations. This paper documents the design, assembly, wind tunnel testing, and comprehensive analysis of its stability and the insights gained from it. The key conclusion is that a hingeless hub, when equipped with swept-tip blades, will significantly increase aeroelastic stability compared with the state-of-the-art gimbaled hub with straight blades. The causes were determined to be the interaction of rotor regressive lag motion with wing–pylon modes and the perturbation of hub pitch and roll moments. The regressive lag was more important at lower speeds, whereas the hub moments were more important at higher speeds. The data shed light on high-speed tiltrotor flight and provided a unique database for validation of advanced rotor comprehensive analysis.

I. Introduction

EFFICIENT vertical takeoff and landing with high-speed cruise remains a valuable area of research. Modern tiltrotors, the current solution to this challenge, are limited to top speeds of 280 kt, which is far short of the aspirational target of 400–450 kt. Tiltrotors are propelled by special rotors that are called proprotors. These rotors act as propellers in airplane mode but have blade flapping and cyclic controls for vertical lift and maneuvering in helicopter mode.

The tiltrotor hub is the heart of the proprotor system, carefully crafted to support both helicopter and airplane modes of flight. Blade and hub flexibility are essential for helicopter mode; however, this aggravates instabilities in airplane mode. A flexible hub, necessary for helicopter-like flight, allows for blade motions both in and out of the plane of the rotor disk. This alleviates high loads in edgewise flight and provides controllability. In contrast, a rigid hub, such as that of a propeller or turbine engine, restricts blade motion. The state-of-the-art tiltrotor hub is a gimbaled hub, which is ideal for reduced loads in helicopter mode. However, this hub requires a thick wing, nominally 23% thickness to chord, for the system to remain free of whirl flutter in airplane mode. The thick wing undermines the promise of high-speed vertical flight due to compressibility drag. This limits the cruise speed to nearly half that of a high-speed propeller aircraft that can afford a much thinner 14% thick wing. To achieve a 450 kt cruise, innovations are needed in hubs and blades so that the wing thickness can be reduced. The hub is the subject of this paper.

The limiting case of the baseline gimbaled hub is a locked gimbal. This results in propeller-like stability, with whirl flutter at speeds far higher than those of a gimbaled-hub tiltrotor. Approaching that limit might generate high oscillatory structural loads in edgewise helicopter-mode flight. This helicopter-mode limiting case is a key difference for tiltrotor and propeller hub designs. Hingeless hubs provide an alternative to the baseline gimbaled hub by introducing stabilizing perturbation hub moments to achieve propeller-like stability in airplane mode with gimbal-like loads in helicopter mode. Despite these advantages, there is a dearth of test data on hingeless hubs, data that might benefit the design of such hubs in the future.

The first documented test of a hingeless tiltrotor was on a 5.5-ft-diameter 1/4.622 Froude-scale model of a Boeing tiltrotor, called the Model 222 (M222). This was performed at the Boeing V/STOL wind tunnel in 1976 [1], but it was not a stability test. The only stability test data publicly available on a hingeless-hub tiltrotor are from its full-scale version, the Boeing 26-ft-diameter Model 222. The M222 was tested at the Ames 40 ft by 80 ft tunnel on a semispan wing in 1972 [2], but its stability data was limited to wing bending modes. The model was tested up to 192 kt. The wing was the same as that of a Bell 25-ft-diameter gimbaled rotor Model 300 that was tested two years earlier [3]. A few years later, the William F. Putnam Company, Princeton, NJ, under contract from the Boeing Vertol Company, Philadelphia, PA, designed and fabricated Froude-scale unpowered models of these rotors as part of NASA Contract NAS 2-8235 (report in June 1975, not in the public domain). The Froude-scaled models had a 2.8 ft diameter and shared the same wing. The models were sent to MIT for gust loads measurements up to 80 kt in the Wright Brothers tunnel [4,5]. These were the first tiltrotor models with interchangeable hubs on the same wing; however, these models have since been destroyed and lost to history. Today, the emergence of electric vertical takeoff and landing aircraft has revitalized the interest in hingeless tiltrotors. However, test data are seldom published, if they are acquired at all, and the limited data that are published are all on performance and loads [6,7]. Often, models are tested without the wing, so flutter tests are out of scope of the test campaign. The objective of this research is to acquire stability data for an interchangeable hub tiltrotor model with larger rotors, modern instrumentation, an electric drive, and high-bandwidth electric actuation.

The Maryland Tiltrotor Rig (MTR), capable of hub interchangeability and equipped with straight and swept-tip blades, has been described in several recent papers [8–15]. There are three other ongoing experimental tiltrotor research projects. Two are in the United States: the NASA Ames Research Center Tiltrotor Test Rig (TTR) [16,17] and the U.S. Army Langley Tiltrotor Aeroelastic Stability Testbed (TRAST) [18–20]. In Europe, the Advanced Testbed for Tiltrotor Aeroelastics (ATTILA) has been developed by the Royal Netherlands Aerospace Center (NLR) [21,22]. The TTR is only focused on performance and loads, not stability. TRAST and ATTILA are semispan tiltrotor models like the MTR but have not focused on advanced geometry swept-tip blades or hingeless hubs.

This paper is focused on the new 4.75-ft-diameter hingeless hub and documents its design, assembly, integration, and testing up to 200 kt on the MTR. This model is loosely Froude-scaled to the Boeing 26-ft-diameter rotor (scale factor, $s = 1/5.47$), at 200 kt that

Received 4 August 2025; accepted for publication 28 December 2025; published online 30 March 2026.

*Graduate Research Assistant, Department of Aerospace Engineering; nobrien2@umd.edu. Student Member AIAA (Corresponding Author).

†Professor, Department of Aerospace Engineering; datta@umd.edu. Associate Fellow AIAA.

corresponds to $200/\sqrt{s} = 468$ kt, although at low helical Mach numbers. The measurements presented are the frequency and damping of wing beam, chord, and torsion motions. Beam motion refers to pylon motion within the plane of the rotor, resulting in bending of the wing in the direction normal to the airfoil surfaces (i.e., up and down). Chord motion refers to pylon motion out of the rotor plane, bending the wing in the chordwise direction. Torsion refers to torque applied to the pylon relative to the wing, resulting in the wing twisting. The first modes of each of these motions are what typically go unstable.

This paper will first summarize the design and integration of the hingeless hub. Then, a short discussion of the pylon center-of-gravity (C.G.) adapter is given. It is used to understand the effect of the pylon C.G. with respect to the wing elastic axis. Then, a description of the wind tunnel test and the postprocessing of the data will be presented. The comprehensive analysis model, built in the in-house University of Maryland Advanced Comprehensive Code–version 2 (UMARC-II), will be presented. Finally, the results will be presented, with beam, chord, and torsion data for the straight and swept-tip blades. Results will be compared with the gimbaled hub, the gimbal-locked hub, and two pylon C.G. locations.

II. Experimental Model

A. Hingeless Hub

The hingeless hub was designed to be fully interchangeable with the baseline gimbaled hub on the MTR. Thus, the dimensions fit the same three-bladed rotor and swashplate dimensions as the gimbaled hub [8,23] and have the same 2 deg precone. There is no kinematic pitch-flap coupling, δ_3, as the effective flap hinge is outboard of the pitch bearing. Without the requirement of a -15 deg δ_3 typically required in a gimbaled hub, there is no geometrical constraint on the pitch link location that currently limits state-of-the-art tiltrotors to three blades. The pitch links remain in the same location, on the retreating side and at the same location, for the sake of interchangeability. This configuration was retained to enable a consistent comparison between the two hubs. The general dimensions of the hingeless hub are shown in Fig. 1.

Designed to be softer in lag motion than the baseline gimbaled hub, the hingeless hub resembles the Boeing M222 frequencies at Mach scale. A specially tailored rectangular flexbeam between the shaft collar and pitch case was designed to make the rotor stiff in-plane (lag frequency > rotational frequency Ω) near the loosely Froude-scale rotational speeds of 1050 revolutions per minute (RPM) ($\Omega = 110$ rad/s), and soft in-plane (lag frequency < rotational frequency Ω) near Mach-scale rotational speeds of 2300 RPM. The rotor rotational frequency is called 1 per revolution, or 1/rev. So stiff in-plane means lag frequency >1/rev and soft in-plane means lag frequency <1/rev. The present paper is limited to a Froude-scale rotor speed of 1050 RPM, so the lag is stiff in-plane. The precise Froude-scale speed for the hingeless hub, based on the hingeless-hub Boeing M222, is 903 RPM. However, there was torsion resonance at 903 RPM (torsion frequency 14.5 Hz = 870 RPM). To avoid this, and for consistency in comparison to the gimbaled hub, the Froude-scale 1050 RPM of the gimbaled hub was used–hence the term "loosely." The gimbaled hub Froude-scale speed was derived from the XV-15 and is sufficiently far from the torsion resonance RPM.

The hub was designed to be clamped on the shaft via a yoke and a clamping nut, as shown in Fig. 2a. The hub arm assembly consists of one thrust and two roller bearings housed between the hub arm and the pitch case, also shown in Fig. 2a. Magnetic pitch encoders are mounted onto the flexbeam for pitch measurements, as shown in Fig. 2b. Once the CAD designs showed proper interchangeability and satisfactory structural properties, the hub parts were fabricated and assembled by the Calspan Corporation. The main component of the hub is made of one AISI 4340 steel piece and is shown in Figs. 3a and 3b. It is made of AISI 4340 steel to provide an adequate factor of safety at the target design frequencies. The pitch bearings, cases, and horns were made identical to the gimbaled hub for interchangeability. These components, assembled onto the hub arm, produced the interchangeable hub that could be reconnected to the same swashplate and drive system as used by the gimbaled hub. The new bearings, pitch cases, and pitch horns are shown in Figs. 3c and 3d.

Instrumentation was also duplicated, including a new set of blade pitch sensors using RLC2IC magnetic encoders and MR080N magnetic incremental rings, both made by the RLS company, as well as pitch link load strain gauges, shaft torque gauges, and blade root strain gauges. This instrumentation was installed after the hub

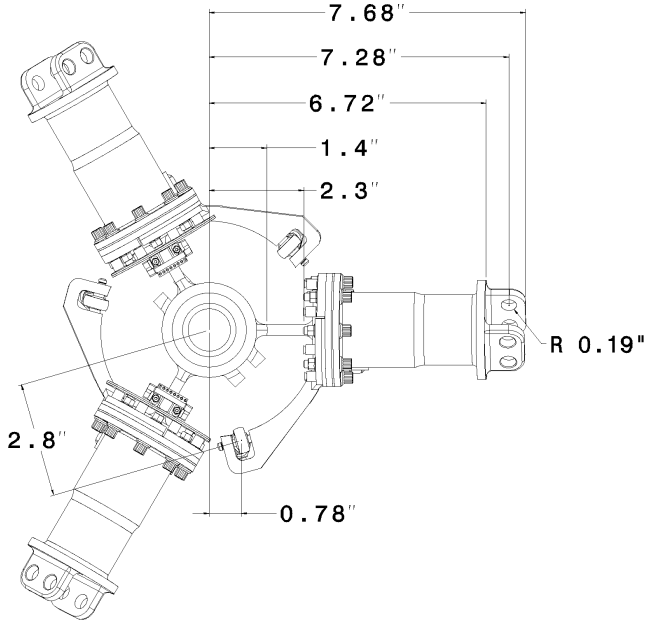

Fig. 1 The hingeless hub top view showing the hub arm, pitch cases, and pitch horns; dimensions in inches.

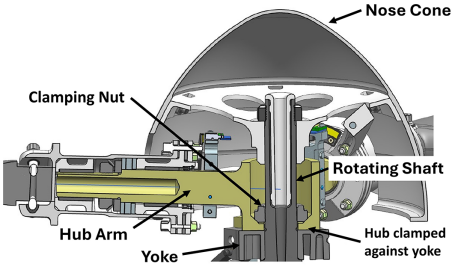

a) Cross sectional view of the hub-shaft connection

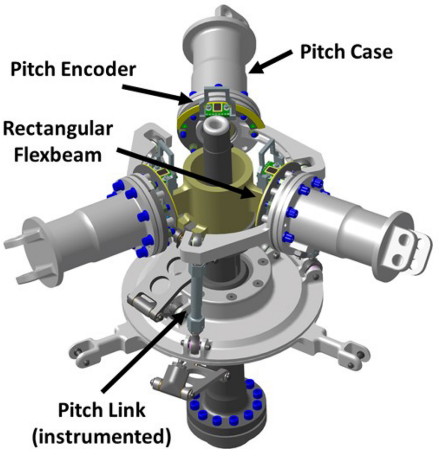

b) Isometric view

Fig. 2 The hingeless hub design.

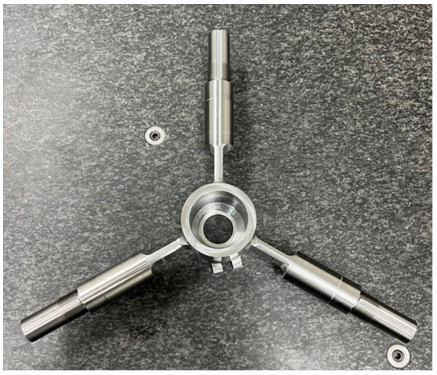

a) Fabricated hub - topview

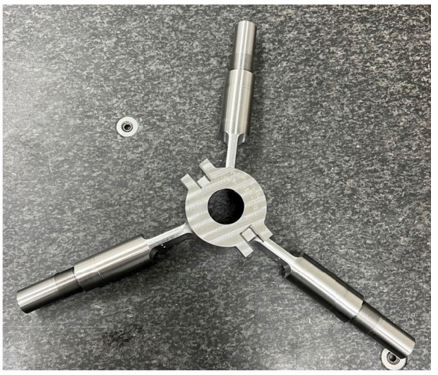

b) Fabricated hub - bottom view

c) Fabricated pitch case and bearing

d) Pitch horn and encoder holder

Fig. 3 Fabricated components of the hingeless hub.

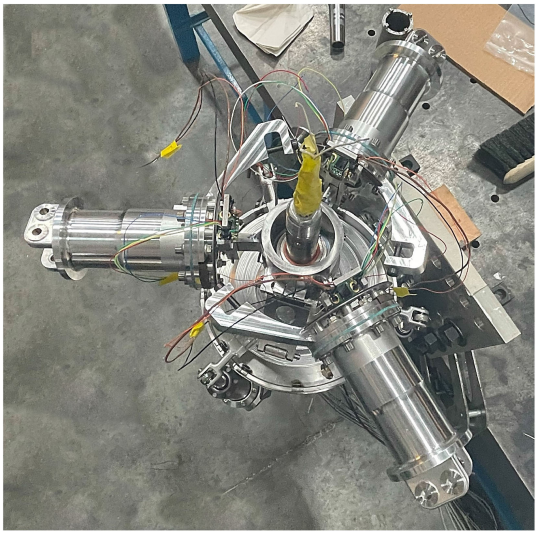

Fig. 4 Hub integrated on rig.

arm components, such as the pitch bearings and pitch cases, were assembled onto the main AISI 4340 steel hub. The hingeless hub was then successfully integrated onto the MTR via the clamping nut and yoke design, as detailed in Fig. 2a and shown in Fig. 4.

B. Pylon Center of Gravity

The pylon C.G. becomes an important parameter when the engine is not tilted [24]. The C.G. location then characterizes the engine placement. The baseline rig, because of the slip ring needed for data acquisition, the load cell, and the electric motor housed inside the pylon, has its C.G. 9.7%R behind the wing spar (which is nominally the elastic axis). This C.G. location does not include the rotor hub and blades, and its rearward position is atypical compared to the 5–15%R forward C.G. location commonly seen in most tiltrotor aircraft. For example, the Boeing 26 ft model had its C.G. ahead by 7.2%R, and the Bell 25 ft model by 6.9%R, without including the rotor hub/blades.

In order to understand the impact of different centers of gravity on a modern hingeless hub tiltrotor, a special adapter plate was built of aluminum to bring the C.G. ahead of the wing spar to 10%R forward. The hingeless hub was tested with and without this adapter. The details of the adapter can be found in Ref. [14].

III. Wind Tunnel Testing

The MTR was tested in the Glenn L. Martin Wind Tunnel at the University of Maryland between January 29 and February 2, 2024. The tunnel has a 7.75 by 11 ft test section and a maximum speed of 200 kt, which translates to Mach 0.3 for sea-level standard conditions. The sphere test of turbulence factor is 1.05, the measured hot-wire intensity is 0.21%, and the floor boundary layer has a displacement thickness of 0.125 in. at the center of the test section. The MTR installed in the Glenn L. Martin Wind Tunnel with the hingeless hub is shown in Fig. 5a. The rig fitted with the C.G. adapter plate to provide the forward C.G. parametric variation is shown in Fig. 5b.

Both swept and straight blades were tested. These blades were fabricated in-house following the procedure laid out in Refs. [10,25]. The blades had a constant chord of 3.15 in., a span of 21 in., a linear twist of −37 deg, and a VR-7 airfoil profile. The layup was ±45 deg relative to the local chord, so there was no material coupling. The swept-tip blades are identical to the straight blades except for a 20 deg sweep at the outer 20%R–a configuration shown to improve wing damping [26,27]. The swept-tip portion had no internal spar, and the airfoils are placed along the swept quarter-chord. The goal of the swept-tip blades was to impact dynamics through aerodynamic pitch-flap coupling. The blades are deliberately kept the same as in the gimbaled hub testing [8,10,14,15] but were refurbished and regauged for the hingeless hub. Details of rotor properties, including properties for swept-tip blades, are listed in Table 1. The rotor radius is 28.5 in., and the distance from the hub to the tunnel floor is 34.05 in. Thus, the rotor tip clearance from the floor is 5.55 in., or 0.195R, which is approximately four times that of the V-22 clearance of 0.053R [28]. This is deliberate to allow for future variations in the rotor radius.

While the rotor and pylon centers of gravity are varied, the properties of the wing were kept constant. These properties are listed in Table 2. The wing airfoil begins about 5.5 in. below the

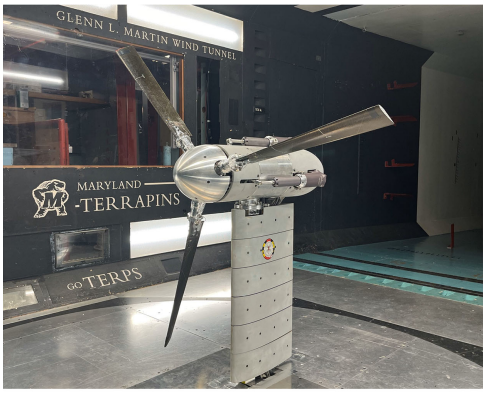

a) Hingeless hub

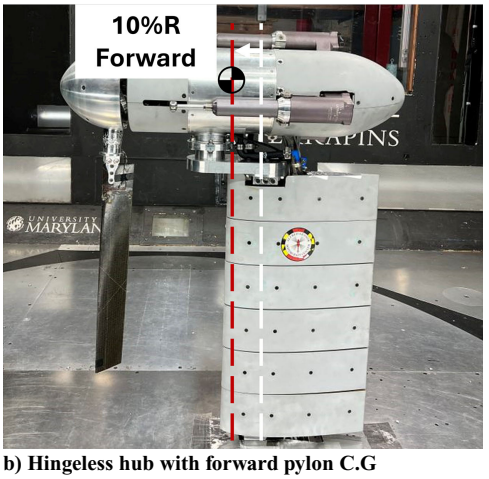

b) Hingeless hub with forward pylon C.G

Fig. 5 Hingeless hub MTR installed in Glenn L. Martin Wind Tunnel.

Table 1 MTR rotor properties

Parameter	Value
No. of blades	3
Radius, R	28.5 in.
Blade chord	3.15 in.
Twist	−37 deg
RPM (Froude)	1050
Rotor airfoil	VR-7
Root cutout	26%R
δ_3	0 deg
Blade sweep	0 deg, 20 deg
Sweep from	0.8R
Floor clearance	0.195R

Table 2 MTR wing–pylon properties

Parameter	Value
Span	27.5 in.
Chord	15.45 in.
Airfoil	NACA 0018
Spar thickness	1.17 in.
Spar chord	2.4 in.
Spar material	Aluminum 6061
Wing weight	23.83 lb
Pylon/rotor weight	66.18 lb
Total weight	90.01 lb
Nominal natural frequencies	
Beam	5 Hz
Chord	9 Hz
Torsion	14.5 Hz
Structural damping	
Beam	0.24%
Chord	1.47%
Torsion	0.30%
Structural damping with adapted C.G.	
Beam	0.80%
Chord	1.45%
Torsion	0.45%

Table 3 Test matrix

Test no.	Speed, kt	Pitch, θ_{75}, deg	RPM	Pylon C.G.
Straight				
U10	30–200	11–57	1050	Standard
U11	30–200	11–58	1050	Forward
Swept-tip				
U12	30–200	11–57	1050	Standard
U13	30–200	11–58	1050	Forward

hub and spans 27.5 in. ending about 1.0 in. from the tunnel floor. The structural damping and frequencies of the installed system (nonrotating and wind-off) were measured by hammer tests. The hingeless hub weight is lower than the gimbaled hub, weighing 7 and 9.18 lb, respectively. The pylon and the blades remain the same, weighing 57 and 2 lb, respectively. The pylon adapter weighed 6 lb and did not change the frequencies and structural damping significantly.

The test matrix is given in Table 3. Four speed sweeps were carried out designated U10–U13. The naming convention follows Ref. [9] with the location, sweep number, and tunnel speed to describe a sweep. For example, N1.78 referred to the test points collected at the Navy tunnel (hence N), in the first speed sweep (hence 1), and at 78 kt. Here, U11.180 would mean test points collected at the University of Maryland (hence U), in the 11th speed sweep at 180 kt.

The tests were conducted in freewheeling mode, in which the rotor system was declutched from the motor. This was accomplished electronically by placing the electric motor in a no-current state to produce a zero-torque condition. Freewheeling is common in tiltrotor tests, as it provides very similar collective pitch but a more conservative whirl flutter boundary. At each speed, the collective pitch was trimmed to achieve the target RPM of 1050. Ideally, hub pitch and roll moments should be zero in axial flow, but blade dissimilarities produced a small moment. As such, the cyclic pitch was trimmed to minimize hub moments. Blade tracking was checked with a strobe light reflecting off colored tape bonded to the blade tips. If the blades were out of track by more than 1/2-thickness, the test was stopped and the pitch links were adjusted.

Once the trim solution was attained, the model was perturbed with high-bandwidth fixed-frame swashplate actuators. While actuating in the fixed frame, the actuation frequencies were kept near the structural wing–pylon natural frequencies identified in the hammer test, in anticipation of flutter frequencies nearby. The wing beam and torsion modes were perturbed using longitudinal cyclic θ_{1s}, and the chord mode was perturbed using the collective θ_0. Five cycles of actuation were introduced, and due to decreasing stroke length at higher frequencies, the pitch perturbation per input voltage had the nominal values of 5.4 deg per volt for the beam mode, 2 deg per volt for the chord mode, and 0.1 deg per volt for the torsion mode. Higher voltage inputs were needed for the chord and torsion inputs due to the higher frequencies. At least three (and up to five) trials were taken for each condition. All three modes had a desired amplitude of perturbation for the system, and efforts were made to keep the perturbations consistent throughout the velocity sweep. This was done to minimize complexity in damping calculations. For example, in beam mode, the goal was a ±200 microstrain reading from the wing beam gauge. At lower speeds, an input voltage of 0.5 V (2.7 deg) was used, while at the top speed of 200 kt, 0.23 V (1.24 deg) was used. Modifications to the input voltage were made throughout the test for all three modes.

IV. Damping Calculation

Wing-mounted strain gauges recorded strains versus time over a period of 10 s at a sample rate of 10 kHz. The record included a portion of the initial steady state, followed by the actuation stage, and then the decay stage. This record was downsampled to 1 kHz for ease of storage.

Damping was calculated from the downsampled signal decay stage using moving block [29,30] and Prony methods [31,32]. Results from the moving block method are primarily shown in this paper to keep the plots readable. A few plots show the Prony results as a comparison. The moving block method assumes that the damped frequency is equal to the natural frequency, that is, $\omega = \omega_n\sqrt{1-\zeta^2} \approx \omega_n$, so it is generally applicable for damping less than 5%, that is, $\zeta \leq 0.05$. Despite this limitation, the advantage of this method is that it is robust to noise. The alternative, at higher damping, is to use Prony. However, it can be quite sensitive to noise. It was important to filter out the per-rev frequencies from blade dissimilarities, even when small, and the noise as much as possible before extraction of damping. The overall scheme is summarized below.

Consider a typical set of wing strain signals from beam, chord, and torsion mode excitation as shown in Figs. 6–8, respectively. These are taken from U11.100, and are used as an example of a challenging case to postprocess. The data were first postprocessed using an infinite-impulse response (IIR) notch filter to remove all per-rev frequencies. Filtering is especially vital for torsion data, as the wing torsion frequency of 14.5 Hz equals 0.83/rev, which is near 1/rev. Blade dissimilarities produce 1/rev forcing, and the torsion signal, already the weakest of all signals due to reduced actuation authority, lies hidden. Low-pass filtering was used to remove higher-order per-rev harmonics, and high-pass filters for lower-frequency motions. For example, when analyzing the torsion signal at 14.5 Hz, the beam response at 5 Hz had a large impact on the waveform but was removed through the use of a high-pass filter. The data after filtering are shown in Figs. 9–11. The steady state, perturbation, and decay are now clearly visible.

The torsion signal from Fig. 11 is replotted in Fig. 12. For the moving block method, a window must be applied to the decay portion of the signal, and a block must move forward each time step to calculate the damping. Within the decay stage, the window must be large enough to adequately capture the decay. In this case, a 1024-sized sample window of 1.024 s ($\Delta t = 0.001$ s) is selected and shown in Fig. 13. Previous work has shown that the block size

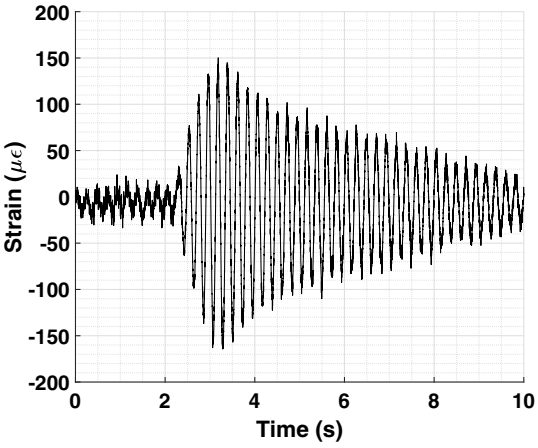

Fig. 6 Beam strain signal.

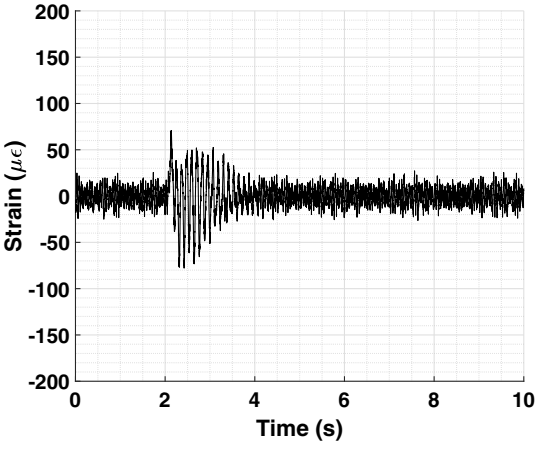

Fig. 7 Chord strain signal.

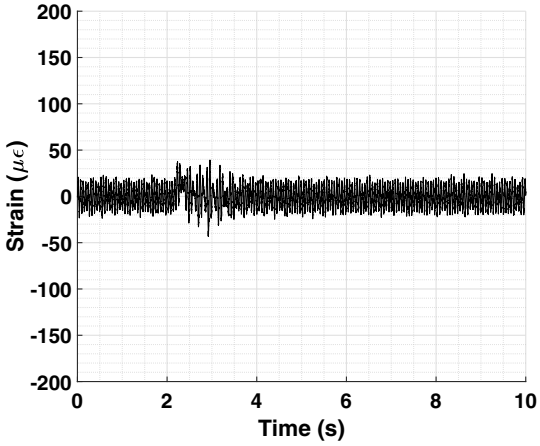

Fig. 8 Torsion strain signal.

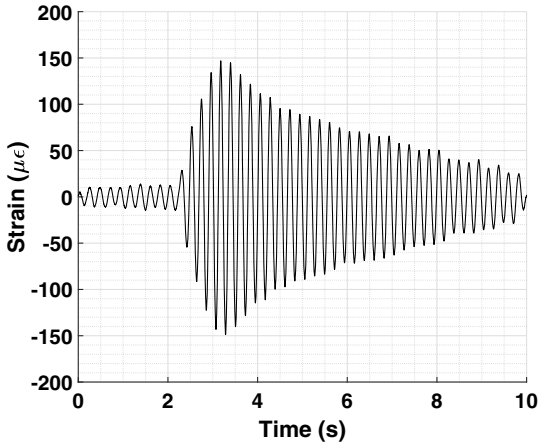

Fig. 9 Filtered beam strain signal.

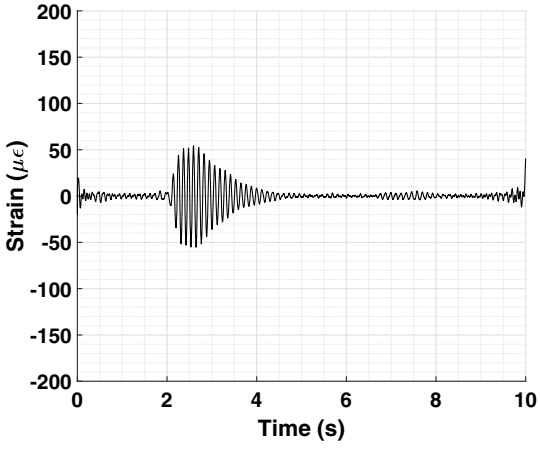

Fig. 10 Filtered chord strain signal.

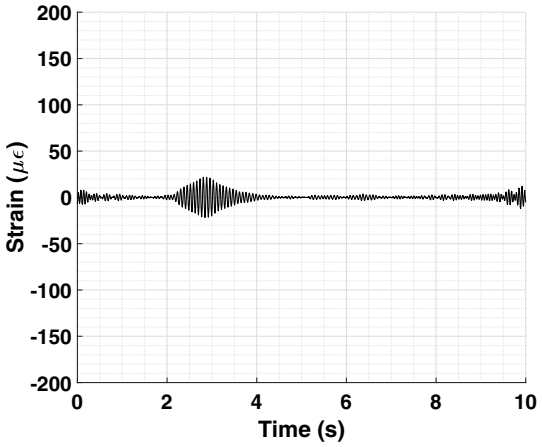

Fig. 11 Filtered torsion strain signal.

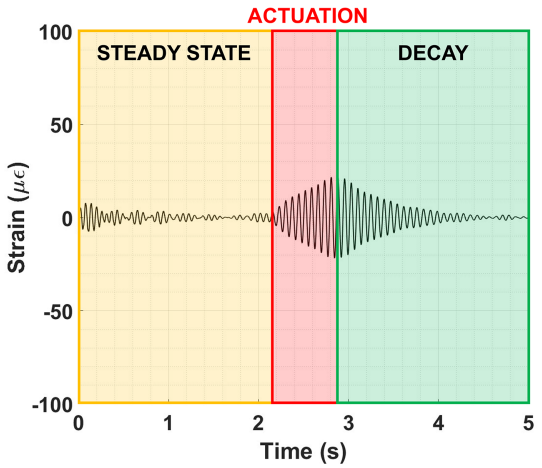

Fig. 12 Torsion strain showing steady-state, actuation, and decay.

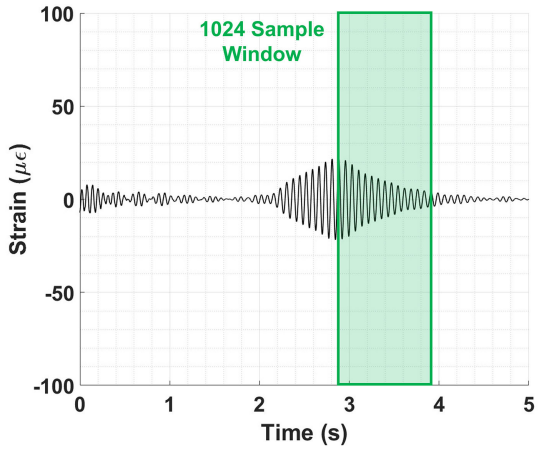

Fig. 13 Decay window.

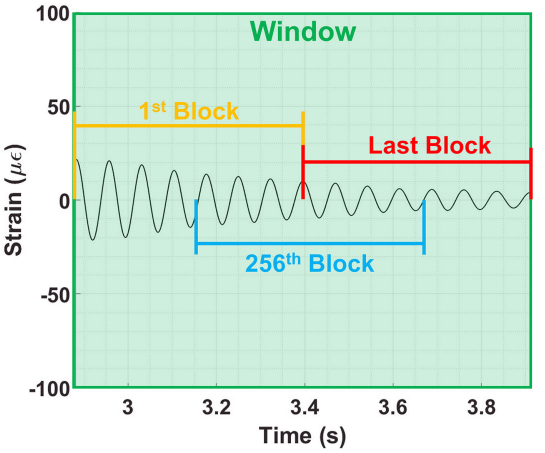

Fig. 14 Moving blocks within decay window.

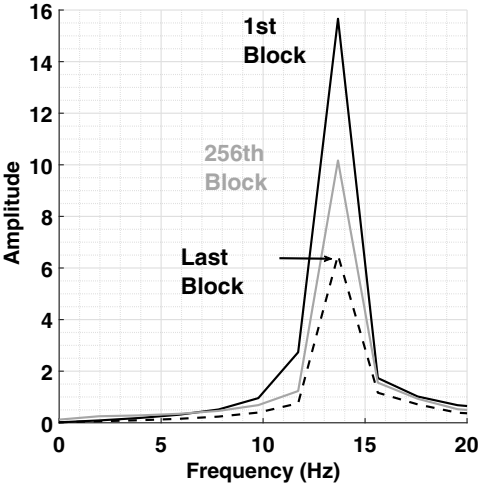

Fig. 15 Amplitude of moving blocks.

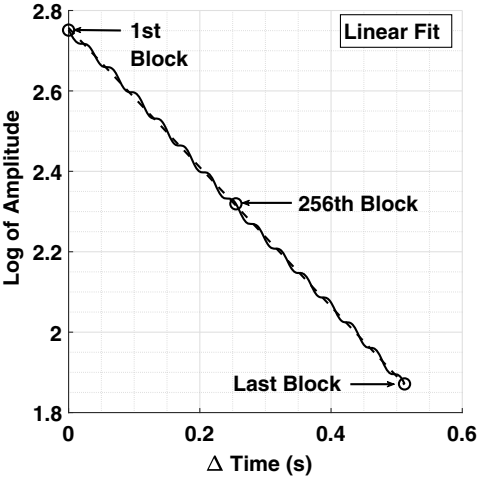

Fig. 16 Natural log of amplitude versus block time.

must be between one-quarter and one-half of the window size, and to compute the fast Fourier transform (FFT) within each block, the block size must be a power of two [30]. Thus, a 512-sized block was chosen, and it is shifted, or moved, along the decay window for each time step from the first to the last possible block. Figure 14 highlights the first, the 256th, and the last block that fits within the 1024-sized decay window. An FFT is performed within each block to find the largest amplitude and corresponding frequency, as shown in Fig. 15. This frequency is the damped frequency, but for low damped cases $\omega_d \approx \omega_n$. The natural log of the amplitude, when plotted versus the starting time of each block, appears as Fig. 16. The slope of the linear fit is $-\zeta\omega_n$, where ζ is the damping ratio and ω_n is the natural frequency. Thus, ζ is calculated. To find the frequency of the decay, an FFT of the full moving block window was taken, and the peak frequency was recorded. This generally matched the damped frequency of each block in the decay.

The Prony method reconstructs a signal with a series of exponential functions that give the form of damped sinusoids. These reconstruct the signal, and the modal number M determines the

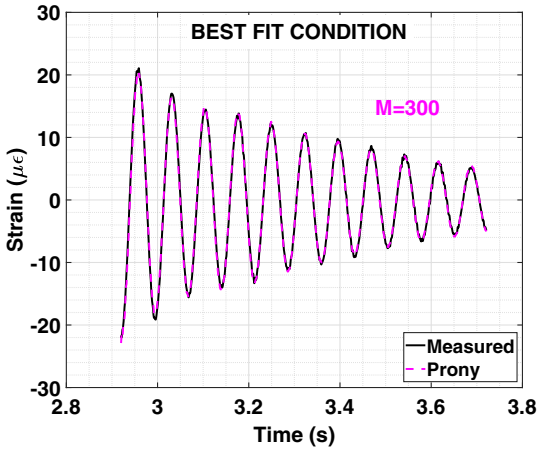

Fig. 17 Prony approximation to torsion signal; $M = 300$.

number of model coefficients of the reconstructed series. In this case, $M = 300$ gave the best regression fit (minimum root mean square error). The result is shown in Fig. 17, with the same torsion signal used in the moving block explanation. In this case, the moving block result was 2.04% damping, and the Prony result was 2.11% damping.

V. Comprehensive Analysis

The University of Maryland Advanced Comprehensive Code–version 2 (UMARC-II) was used as the baseline analysis platform [11,33] and refined for this study to model the MTR. The system properties input into the model, the mathematical modeling, and the solution procedure are summarized below.

A. Properties

The blade mass and stiffness properties were measured in-house. The root-end properties were calculated using commercial FEA. The pylon moments of inertia have yet to be measured with the new hub, so the gimbaled values given in Ref. [9] were retained. Despite this inaccuracy in the model, the large inertia of the pylon is expected to make this discrepancy in the model have negligible effects on the results. The mass was updated to reflect the hingeless hub. The wing spar structural properties were calculated based upon geometry and material properties, and the measured structural damping in Table 2 was used. The airfoil properties of the VR-7 blade and NACA0018 wing were obtained from in-house CFD as a C-81 deck. In the experimental model, the wing is segmented, which is typical of a tiltrotor flutter model. It is considered aerodynamically continuous in the analysis. The segmented wing allows friction to occur should sudden instabilities appear, but the gaps are small enough to prevent three-dimensional flows.

B. Model

Because the layup is quasi-isotropic, isotropic Euler–Bernoulli beam finite elements suffice to model the rotor. Each blade was modeled with 18 elements. Figure 18 and Table 4 list these properties. Note that for the swept-tip blades, the values reduce from 80%R to 100%R due to the swept section lacking a spar. The reduced values are mass per length 0.15 kg/m, normal bending stiffness $EI_n = 12\ \mathrm{N \cdot m^2}$, chordwise bending stiffness $EI_c = 534\ \mathrm{N \cdot m^2}$, and torsional stiffness $GJ = 36.8\ \mathrm{N \cdot m^2}$. The rotor fan plot (with straight blades) is shown in Fig. 19. The hingeless frequencies are shown with solid lines. For validation of the model, vacuum chamber test data are used. This test used the same rotor blades as the MTR but had a rigid hub replicating the gimbal-locked hub. Predictions are shown as dashed lines. There is good agreement with

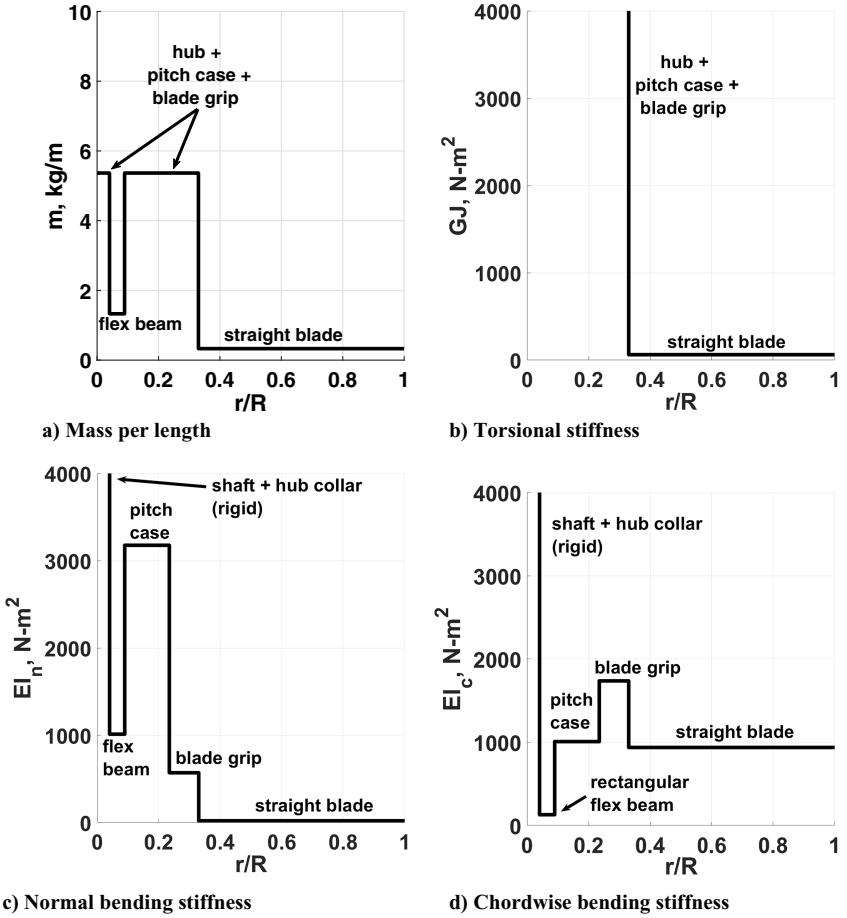

a) Mass per length

b) Torsional stiffness

c) Normal bending stiffness

d) Chordwise bending stiffness

Fig. 18 Structural properties of the hingeless rotor.

Table 4 MTR rotor model properties

Property	Shaft/collar (0–0.041 *r/R*)	Flex beam (0.041–0.09 *r/R*)	Pitch case (0.09–0.23 *r/R*)	Blade grip (0.23–0.33 *r/R*)	Blade (0.33–1 *r/R*)
Mass per unit length, kg/m	5.37	1.33	5.37	5.37	0.33
Torsional stiffness, GJ, N · m^2	Rigid	Rigid	Rigid	Rigid	62
Normal bending stiffness, EI_n, N · m^2	Rigid	1012	3177	570	20
Chordwise bending stiffness, EI_c, N · m^2	Rigid	128	1007	1737	937

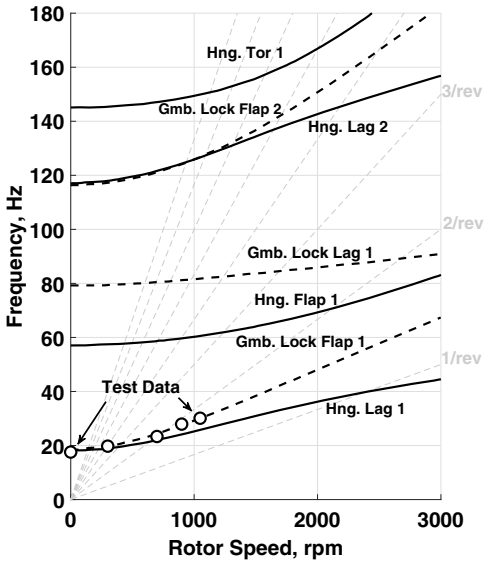

Fig. 19 Hingeless hub at 40 deg collective.

the test data [25]. The hingeless hub is harder to reproduce in the vacuum chamber rotor rig due to its unique flexbeam design intended to achieve the desired lag frequency. Despite these differences, because the blades are identical, the model is considered validated. At 1050 RPM, the lag frequency for the hingeless hub is around 1.6/rev, and the flap frequency 3.5/rev. At 2400 RPM, the lag mode would cross over from stiff- to soft-inplane, and the flap frequency would be around 1.8/rev.

The wing is isotropic. The wing itself is modeled with 10 elements. The adapter plate was simply modeled as a C.G. shift. The mass and inertia of the adapter plate are not included in this preliminary model, as the large mass and inertia of the pylon make the adapter mass and inertia insignificant for damping predictions. The pylon and hub connection are modeled with two structural elements.

A lifting-line aerodynamic model is used, with uniform inflow for the wake. The induced inflow is approximately zero in airplane mode, so a refined wake model is usually not needed. Analysis with free wake confirmed that there was no effect of the wake [11,33]. Linear unsteady aerodynamics is used for both the rotor and wing. It is not needed on the wing (as the reduced frequency is quite low) but retained nevertheless for consistency with the rotor.

C. Solution Procedure

First, the rotor is trimmed in the freewheeling condition; the collective is found for zero torque at the tunnel speed. The predicted and measured collectives are compared in Fig. 20. The measurements are similar for all blades, with satisfactory comparisons to the predictions.

Once trimmed, eigenanalysis is used to find the stability roots. The rotor equations are converted to multiblade coordinates to allow eigenanalysis. The solution was verified with a transient analysis with the rotor equations in the rotating frame. The transient option is easier for the gimbaled hub but would not produce a solution if the model were to be unstable.

VI. Results

A. Measured Damping

The damping from the baseline model is shown in Fig. 21. The baseline model is with straight blades and without the pylon C.G. adapter. The beam damping is the lowest, with an increasing trend with speed and a drop-off as it approaches 200 kt. The next higher mode is torsion, with a relatively flat trend. Finally, there is chord damping, which is the highest, with a rapidly decreasing trend between 30 and 100 kt and relatively flat thereafter.

A curious change in behavior is noticed when the straight blades are replaced with swept-tip blades. The damping is shown in Fig. 22. The chord and the torsion are now flipped. The chord is now the next higher mode from the beam, with a relatively flat trend, whereas torsion has the highest damping, with a rapidly decreasing trend between 30 and 100 kt. Note that all other parts of the model remained the same; only the blades were replaced. The blades were identical as well, except for the swept tip.

The C.G.-shifted configuration changes the results but not the fundamental behavior. The beam damping is still the lowest,

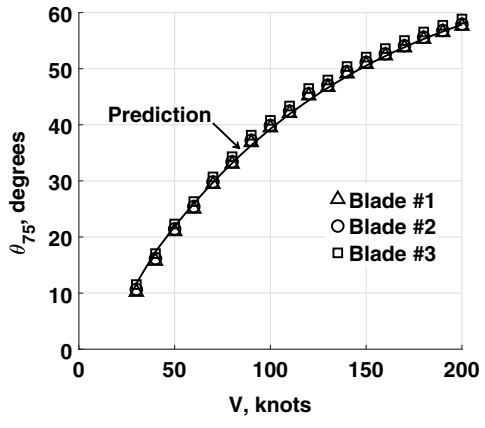

Fig. 20 Measured and predicted collective pitch.

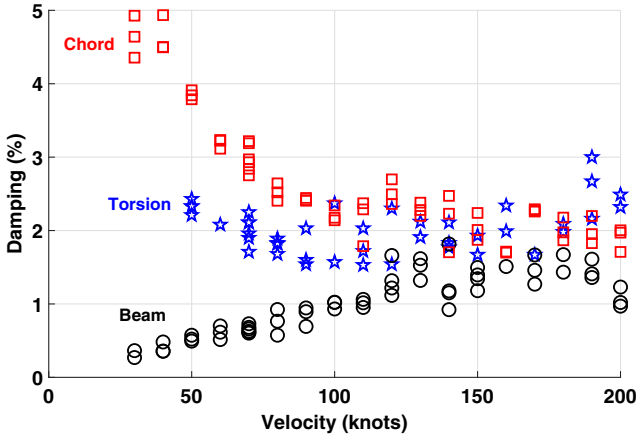

Fig. 21 Damping; straight blade.

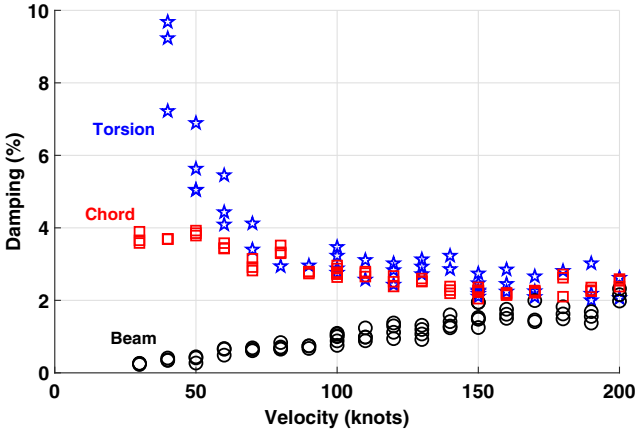

Fig. 22 Damping; swept-tip blade.

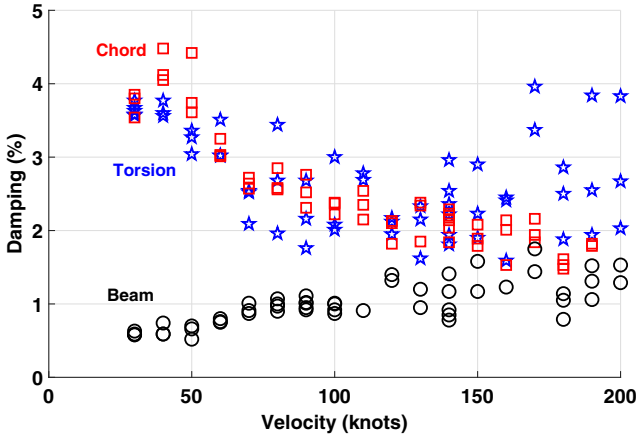

Fig. 23 Damping; straight blade, pylon C.G. 10%R forward of wing spar.

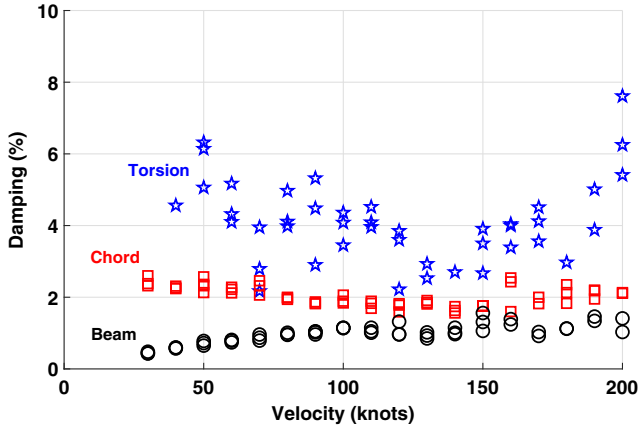

Fig. 24 Damping; swept-tip blade, pylon C.G. 10%R forward of wing spar.

and chordwise damping remains high, as shown in Fig. 23. The swept tip again flips the behavior of the chord and torsion, bringing the torsion up and the low-speed chord damping lower (Fig. 24). One change in the nature of the measurements appears to be a large amount of scatter in the torsion data. There also seems to be a general rise in torsion damping at high speed, although precise conclusions are premature with this level of scatter.

The curious behavior of the chord and torsion flipping trends is explained by comparing measured data with UMARC-II predictions in the following section.

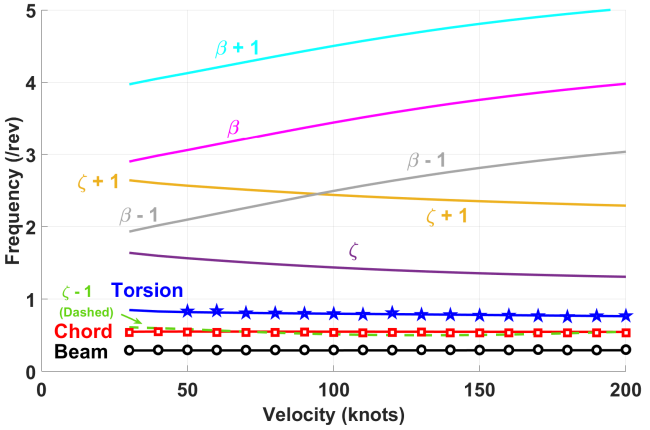

Fig. 25 Predicted frequencies (solid) versus test data (symbols); straight blades, baseline C.G.

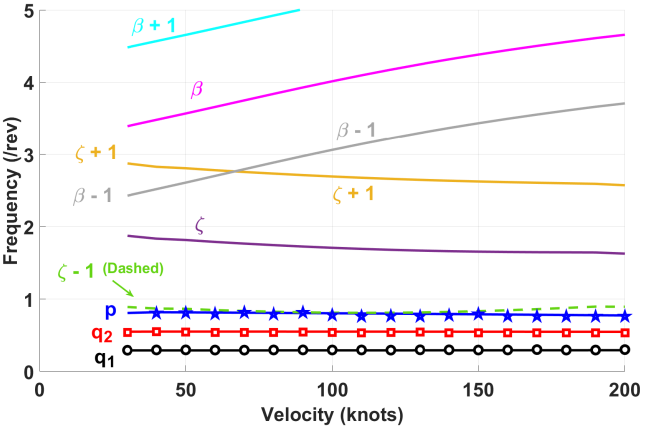

Fig. 26 Predicted frequencies (solid) versus test data (symbols); swept-tip blades, baseline C.G.

B. Data Versus Predictions

The comprehensive analysis can be used to gain insights into what is driving the stability characteristics of the hingeless hub. Predictions also provide a preliminary check of the data as well as validation for the analysis.

Consider the baseline configuration first–baseline C.G. and straight blades. The predicted frequencies are shown in Fig. 25. The wing–pylon beam mode is denoted as q_1, chord as q_2, and torsion as p. These are coupled aeroelastic frequencies but are labeled according to the dominant structural mode. The test data are shown as symbols and predictions as lines. The frequencies remain well separated throughout. The rotor flap (first mode) and lag (first mode) frequencies are those of corresponding multiblade coordinates. The standard notations of β and ζ denote the collective flap and lag, respectively. So $\beta + 1$ and $\zeta + 1$ are the high-frequency flap and lag modes, signifying flap frequency $+\Omega$ and lag frequency $+\Omega$, respectively. Similarly, $\beta - 1$ and $\zeta - 1$ are the low-frequency flap and lag modes, signifying flap frequency $-\Omega$ and lag frequency $-\Omega$, respectively. These frequencies are hard to measure, as they are well damped and in the rotating frame; hence, predicted values play a key role in fundamental understanding. It is clear that the low-frequency lag mode (in this case regressive) is very close to the chord mode. The lag mode is very well damped in airplane mode due to high inflow, and this damping is transferred to the chord mode.

Now consider the swept-tip blades. The predicted frequencies are shown in Fig. 26. The sweep at the tip provides greater stiffness in lag motion due to lower mass and a larger restoring moment from centrifugal force. This increases the lag frequency so that the regressive lag is now closer to the torsion mode. Therefore, the damping is now transferred to the torsion mode. This explains the

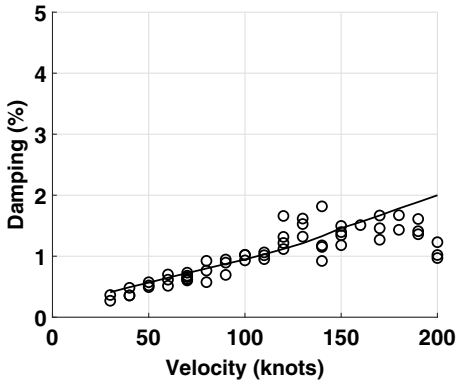

Fig. 27 Beam damping; straight blade.

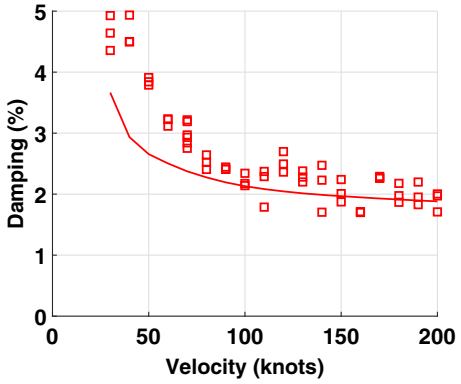

Fig. 28 Chord damping; straight blade.

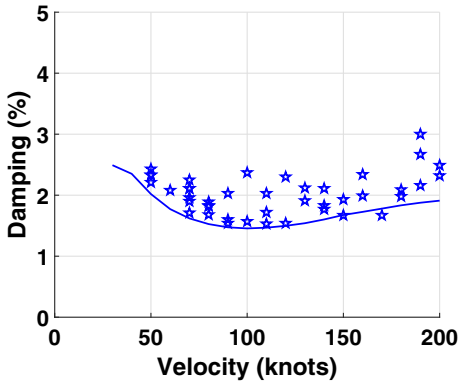

Fig. 29 Torsion damping; straight blade.

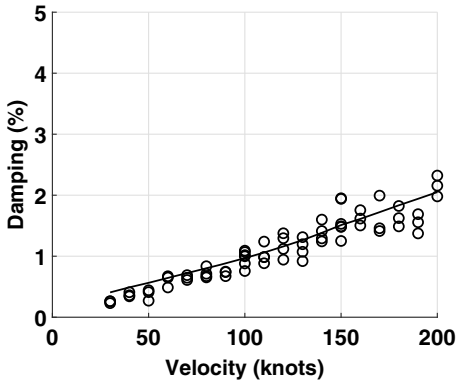

Fig. 30 Beam damping; swept-tip blade.

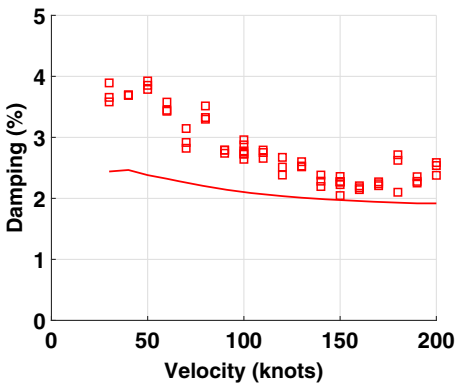

Fig. 31 Chord damping; swept-tip blade.

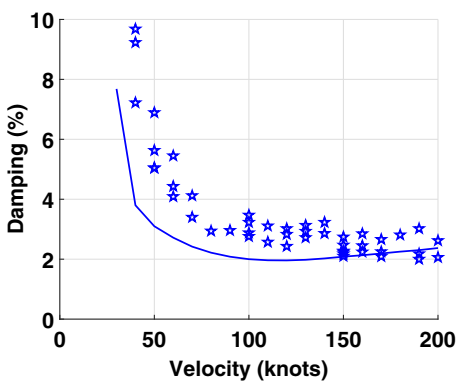

Fig. 32 Torsion damping; swept-tip blade.

curious behavior of the chord and torsion modes flipping. This also shows that a swept tip can have other effects beyond pitch–flap coupling alone. Attention is focused next on damping.

Consider first the baseline configuration again. The beam, chord, and torsion damping modes are shown in Figs. 27–29, respectively. Beam predictions are satisfactory up to 180 kt, but the drop that appears to occur at 190 kt and continues to 200 kt is not predicted at all. The chord damping behavior is captured, which confirms that our data show the effects of the regressive lag interaction. However, the magnitude of the prediction at low speeds is not satisfactory. The torsion damping predictions are reasonable, capturing the downward trend up to 120 kt followed by a gradual increase. There is a slight underprediction across all speeds.

Now consider the swept-tip configuration again. Figures 30–32 once again show the beam, chord, and torsion damping and predictions, respectively. Beam mode predictions are similar to the baseline blades and are satisfactory across all speeds. The drop in damping around 200 kt is no longer observed. Now to focus on the chord and torsion modes. Frequency predictions have shown that the swept-tip regressive lag mode proximity to the wing chord is now gone. Thus, neither the data nor the predictions show the peak in damping at low speeds in the chord mode. The magnitude error remains, so the predictions are not very satisfactory. The regressive lag is closer to the torsion mode. The sharp rise in damping at lower speeds due to this proximity is predicted by the analysis. Note that the y-axis has a higher scale to capture the increase in damping.

The major discrepancies in the predictions are due to underpredictions for both the straight- and swept-tip blades' chordwise data sets and the torsion mode in the swept-tip blades. This could be due to a failure to capture the full stabilizing effects due to the regressive lag interaction with the wing modes, as the low-speed peaks seen in Figs. 28 and 32 reflect the trend but not the magnitude.

Next consider the C.G.-shifted configuration in the same sequence, first the straight blades, then the swept tip. The beam,

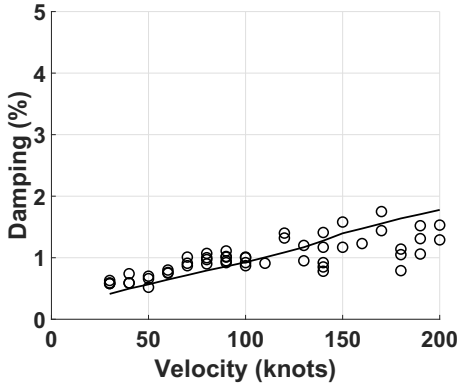

Fig. 33 Beam damping; straight blades; C.G. shifted.

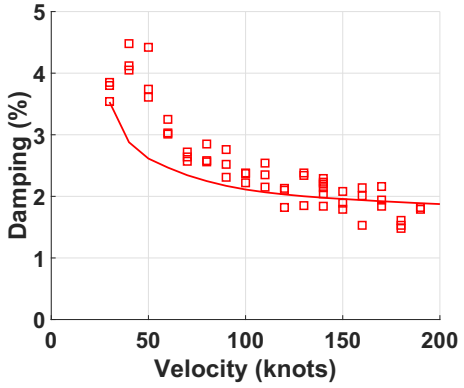

Fig. 34 Chord damping; straight blades; C.G. shifted.

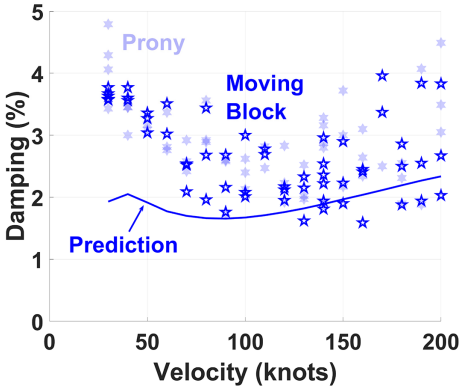

Fig. 35 Torsion damping; straight blades; C.G. shifted.

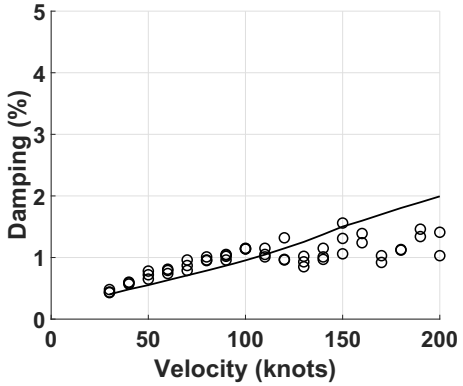

Fig. 36 Beam damping; swept-tip blades; C.G. shifted.

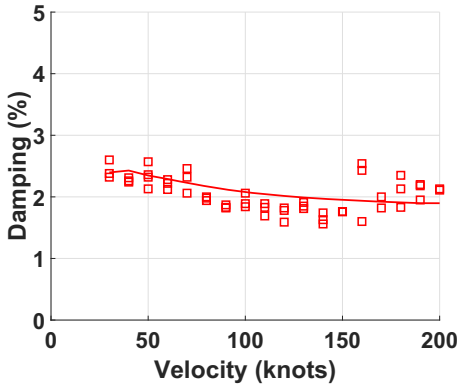

Fig. 37 Chord damping; swept-tip blades; C.G. shifted.

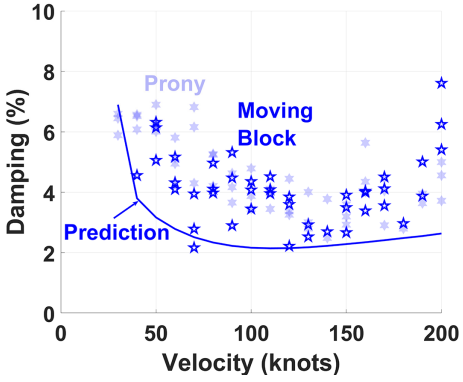

Fig. 38 Torsion damping; swept-tip blades; C.G. shifted.

chord, and torsion damping for the straight blades are shown in Figs. 33–35, respectively. There is no major change in beam and chord results, with moderately acceptable predictions throughout the velocity range. The problem is with torsion and its high amount of scatter. The data are shown extracted with two different methods, Prony and moving block, and both show this high scatter. Nevertheless, the damping is higher at low speeds than in the standard C.G. configurations. The analysis does not pick up these trends; the predicted damping remains the same as before (Fig. 29). Perhaps this suggests that the adapter piece must be modeled properly, with inertia, stiffness, and vertical displacement, and not just considered a C.G. offset.

The beam, chord, and torsion damping for the swept-tip blades are shown in Figs. 36–38, respectively. Recall, the principal change in physics is the shift of the regressive lag toward torsion. Because it is well predicted, there appears to be less problem with torsion. The data in torsion still show a high scatter, although the Prony analysis appears to show a little less scatter. Even though the trend is captured, the magnitudes are underpredicted throughout the speed range. Note that the *y*-axis has a larger scale.

Overall the baseline C.G. predictions are good, and the use of comprehensive analysis gives us a fundamental understanding of the interesting behavior of the damping, namely, the damping increase due to the highly damped regressive lag interaction with the wing chord and torsion modes for the straight and swept-tip blades, respectively. The forward-shifted C.G. data and predictions show the need for improvement in both the comprehensive analysis and data acquisition in the future.

C. Fundamental Understanding

To gain a clearer understanding of how a hingeless hub compares with the current state-of-the-art gimbaled hub, three parametric variations are studied: 1) hingeless versus gimbaled hub, 2) hingeless versus gimbal-locked hub, and 3) straight versus swept-tip

blades. The baseline pylon C.G. location is considered for all. The hingeless hub results are new here. The gimbaled and gimbal-locked results are reproduced from Refs. [13,32].

1. *Hingeless Versus Gimbaled Hub*

Consider straight blades. Figures 39–41 compare damping in beam, chord, and torsion modes, respectively. In the beam mode there is no significant change. In the chord and torsion modes the changes are significant. This is generally expected, as the hub moments would affect these modes—hub roll (or airplane yaw) affecting chord and hub pitch (or airplane pitch) affecting torsion. In the chord mode, the impact is positive—the damping increases. In the torsion mode, the impact is negative—the damping decreases. Thus, overall, the hingeless-hub MTR would be more stable than its gimbaled counterpart, except for the decrease in torsion mode stability. The increase in damping in chord mode was explained earlier by its proximity to the regressive lag. (The regressive lag of the gimbaled hub is far away from the chord mode.) But how much is the contribution from the hub moment? This is established in the following section.

2. *Hingeless Versus Gimbal-Locked Hub*

To understand the relative contributions of lag and hub (roll) moment, the hingeless hub data are compared with the gimbal-locked hub. The gimbal-locked hub produces hub moments, but the regressive lag is far away from the chord mode; thus, only the hub roll moment effect would kick in.

First, compare the beam modes shown in Fig. 42. There is no significant change once again, which is to be expected, as the hub roll moment and regressive lag interaction are not present in the beam mode. However, the hub roll moment does affect the chord mode. Figure 43 shows the chord damping. It is clear that locking the gimbal does not have the same effect as the hingeless hub. It

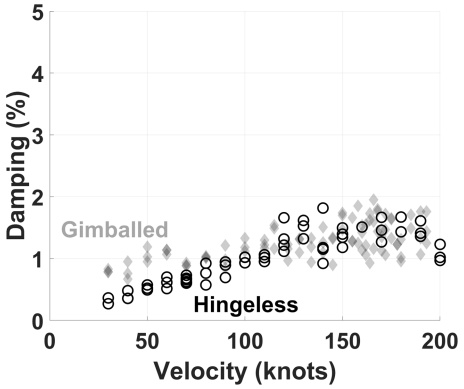

Fig. 39 Beam damping; hingeless versus gimbaled.

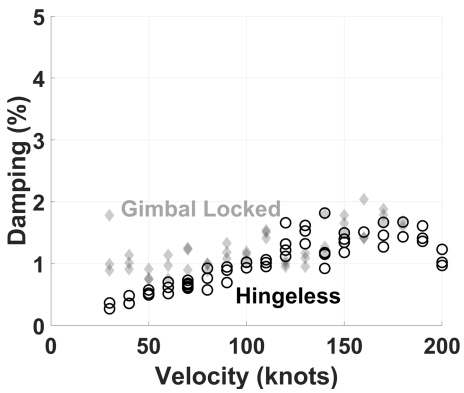

Fig. 42 Beam damping; hingeless versus gimbal-locked.

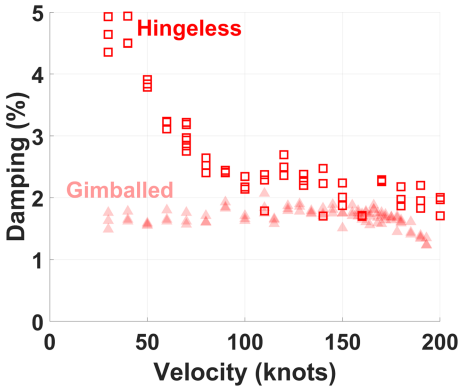

Fig. 40 Chord damping; hingeless versus gimbaled.

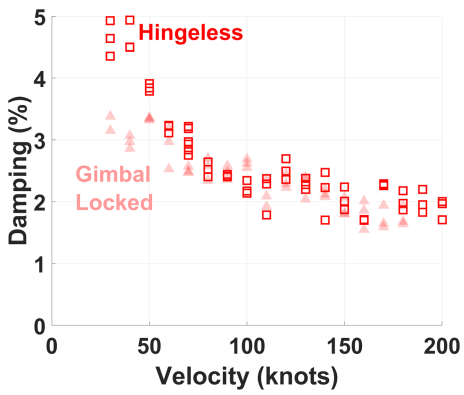

Fig. 43 Chord damping; hingeless versus gimbal-locked.

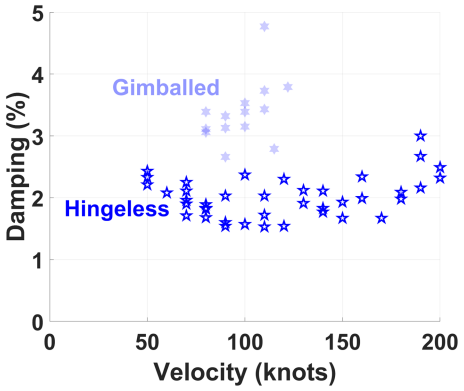

Fig. 41 Torsion damping; hingeless versus gimbaled.

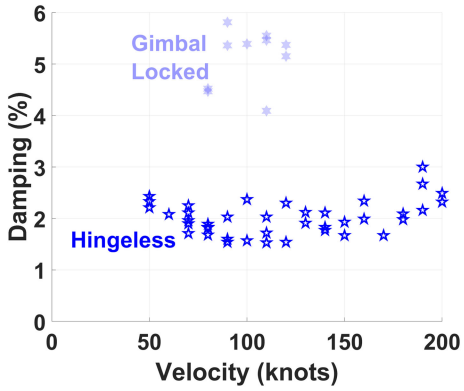

Fig. 44 Torsion damping; hingeless versus gimbal-locked.

appears to produce only about half the damping increase of the hingeless hub, at least at the low speeds. This implies that only half the damping increase is from the hub moment; the other half is from the regressive lag. At higher speeds, beyond 80 kt or so, locking the gimbal produces almost the same damping as the hingeless hub. This implies that the damping is then mainly from the hub moment at higher speeds. The torsion results shown in Fig. 44 are similar to the gimbaled versus hingeless hub. Once again, there is a marked decrease in stability where comparable.

3. *Straight Versus Swept-Tip*

The hingeless hub data are now compared between the straight and swept-tip blades. Figures 45–47 compare damping in beam, chord, and torsion modes, respectively. In the beam mode, there is no significant change. At 200 kt, there appears to be an increase in damping, but conclusions may be premature with a single set of data points. In the chord mode, there is no significant change either. The hub roll moment is influencing both sets of blades, and the regressive lag is closer to the wing chord mode for both sets of blades—straight or swept—when compared to the gimbaled hub. However, for the swept-tip blades, the regressive lag mode is right on top of the wing torsion mode. This highly damped mode drives up the stability of the swept-tip blades on the hingeless hub, as shown in Fig. 47. The damping of the torsion mode increases significantly under 100 kt. This alleviates the lost torsional stability compared to the gimbaled hub. This change, brought about by introducing the swept-tip blades, only affects the hingeless hub. When in the gimbaled hub configuration, there was no change in the damping results when the swept-tip blades were introduced [15]. Thus, in summary, the hingeless hub with the swept-tip blades appears to have the most damping.

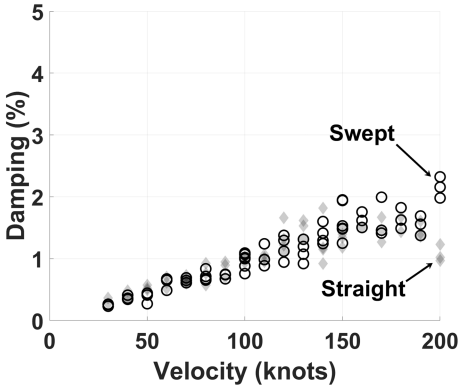

Fig. 45 Beam damping; swept versus straight blades.

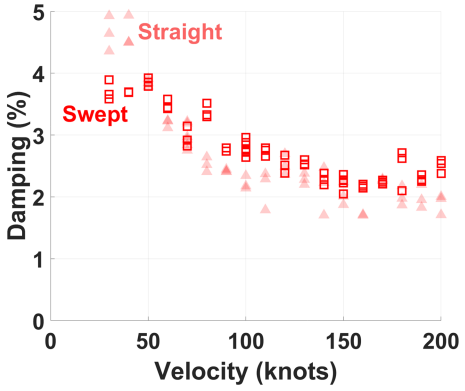

Fig. 46 Chord damping; swept versus straight blades.

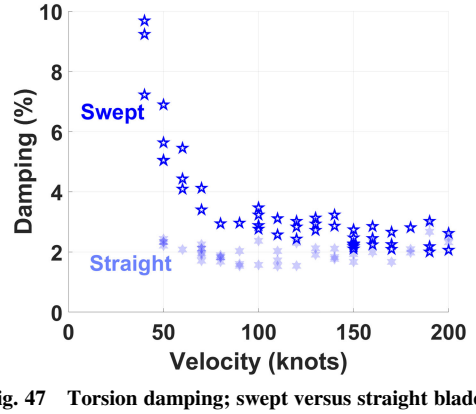

Fig. 47 Torsion damping; swept versus straight blades.

VII. Conclusions

A 4.75-ft-diameter Froude-scaled hingeless hub tiltrotor model was developed and tested up to unprecedented speeds of 200 kt (corresponding to 468 kt full scale) at the University of Maryland Glenn L. Martin Wind Tunnel. The model had interchangeable hubs, blades, and pylon centers of gravity, allowing several important parametric variations that are hard to achieve in full-scale flight tests. Straight and swept-tip blades were tested, and the pylon C.G. was moved aft and forward of the wing elastic axis. Beam, chord, and torsion mode damping were measured for all cases. Based on this work, the following key conclusions are drawn:

1) The hingeless hub, when equipped with swept-tip blades, has significantly higher stability than a gimbaled hub with straight blades.

2) The hingeless hub, with baseline straight blades, has higher stability in the chord mode than the gimbaled hub. The chord stability is more than twice at speeds lower than 100 kt and about 50% higher at 200 kt.

3) The interaction of the rotor low-frequency lag with the wing modes, chord for straight and torsion for swept, is the primary mechanism behind the increase in stability.

4) The stability in beam mode is comparable between the two hubs. Neither perturbation hub moments nor low-frequency lag interact with this mode.

5) Comprehensive analysis was able to capture the general trends for the hingeless hub cases, but the magnitudes were off by up to 50%. Predictions were harder for the torsion mode and swept-tip blades. It captured the subtle low-frequency regressive lag interactions with wing chord and torsion modes and how they changed with swept-tip blades.

6) The stability remained largely unaffected between pylon C.G. forward or backward. The forward C.G. case showed very high levels of scatter in the torsion mode for reasons unclear at present.

Acknowledgments

This work was carried out at the Alfred Gessow Rotorcraft Center, University of Maryland at College Park, under the Army/Navy/NASA Vertical Lift Research Center of Excellence (VLRCOE) grant number W911W62120003, with technical monitoring from Mahendra Bhagwat and points of contact Tom Parham (Bell), Hyeonsoo Yeo and Seyhan Gul (Army), and Wayne Johnson (NASA). Fabrication and assembly were carried out with the assistance of Dave Privett of the Calspan Corporation and the use of a Tormach six-axis CNC. We also wish to thank Benjamin Strobel, Joseph Hussey, and John Shinkle of the Glenn L. Martin Wind Tunnel.

References

[1] Magee, J. P., and Alexander, H. R., "Wind Tunnel Test on a 1/4.622 Froude Scale, Hingeless Rotor Tilt Rotor Model Volumes I–IV," NASA CR 151936-151939, Sept. 1976.

[2] Magee, J. P., and Alexander, H. R., "V/STOL Tilt Rotor Aircraft Study: Wind Tunnel Tests of a Full Scale Hingeless Prop/Rotor Designed for the Boeing Model 222 Tilt Rotor Aircraft," NASA CR D222-100059-1, April 1973.

[3] Helicopter, B., "Advancement of Proprotor Technology, Task II-Wind-Tunnel Test Results (NASA Contract NAS 2-5386)," NASA CR 114363, 1972.
[4] Ham, N. D., Bauer, P., Lawrence, T., and Yasue, M., "A Study of Gust and Control Response of Model Rotor-Propellers in a Wind Tunnel Airstream," NASA CR 137756, Aug. 1975.
[5] Ham, N. D., and Whiteaker, H., "A Wind-Tunnel Investigation of Tilt-Rotor Gust Alleviation System," NASA CR 152264, Jan. 1978.
[6] Staruk, W., Kelly, S. P., Bain, J., Bleu-Laine, M.-H., Escobar, D., Krishnan, M., Lister, J., Sprecher, E., Thai, A., Thomas, J., et al., "Overview of Wind Tunnel Testing of the Joby Aviation eVTOL Isolated Propeller System," *Vertical Flight Society's 81st Annual Forum*, Vertical Flight Soc., Fairfax, VA, May 2025, pp. 1–15. https://doi.org/10.4050/F-0081-2025-392
[7] Escobar, D., Staruk, W., Thomas, J., and Trembois, N., "Comparison of Performance and Blade Loads Analytical Predictions with Wind Tunnel Measurements of a Joby Aviation eVTOL Propeller," *Vertical Flight Society's 81st Annual Forum*, Vertical Flight Soc., Fairfax, VA, 2025, pp. 1–19. https://doi.org/10.4050/F-0081-2025-153
[8] Datta, A., Tsai, F., and Sutherland-Foggio, J., "Design of a New Tiltrotor Test Facility at the University of Maryland," *AIAA Scitech 2019 Forum*, AIAA Paper 2019-2136, 2019. https://doi.org/10.2514/6.2019-2136
[9] Tsai, F., Sutherland, J., Akinwale, A., Morin, A., Gul, S., and Datta, A., "Development and Whirl Flutter Test of the Maryland Tiltrotor Rig," *Journal of the American Helicopter Society*, Vol. 69, No. 1, Jan. 2024, pp. 1–15. https://doi.org/10.4050/JAHS.69.012009
[10] Sutherland, J., Tsai, F., and Datta, A., "Whirl Flutter Test of Swept-Tip Tiltrotor Blades," *Journal of the American Helicopter Society*, Vol. 69, No. 1, Jan. 2024, pp. 1–12. https://doi.org/10.4050/JAHS.69.012010
[11] Gul, S., and Datta, A., "Prediction and Validation of Whirl Flutter Data of the Maryland Tiltrotor Rig," *Journal of the American Helicopter Society*, Vol. 69, No. 1, Jan. 2024, pp. 1–11. https://doi.org/10.4050/JAHS.69.012011
[12] Akinwale, A., and Datta, A., "Understanding High-Speed Aeroelastic Stability of a Gimballed Proprotor," *Journal of Aircraft*, Vol. 62, No. 2, March–April 2025, pp. 313–327. https://doi.org/10.2514/1.C037994
[13] Delgado, X., and Datta, A., "High Speed Whirl Flutter Tests of Swept-Tip Rotor Blades," *AIAA SCITECH 2024 Forum*, AIAA Paper 2024-1851, 2024. https://doi.org/10.2514/6.2024-1851
[14] Akinwale, A., and Datta, A., "The Effect of Pylon Center of Gravity on Tiltrotor Whirl-Flutter," *AIAA SCITECH 2025 Forum*, AIAA Paper 2025-0429, 2025. https://doi.org/10.2514/6.2025-0429
[15] Delgado, X., and Datta, A., "High Speed Whirl Flutter Tests and Predictions of Swept-Tip Tiltrotor Blades," *AIAA SCITECH 2025 Forum*, AIAA Paper 2025-0428, 2025. https://doi.org/10.2514/6.2025-0428
[16] Acree, C., Sheikman, A., and Norman, T., "High-Speed Wind Tunnel Tests of a Full-Scale Proprotor on the Tiltrotor Test Rig," *Vertical Flight Society 75th Annual Forum*, Vertical Flight Soc., Fairfax, VA, May 2019, pp. 1–19. https://doi.org/10.4050/F-0075-2019-14736
[17] Acree, C., "Vertical Climb Testing of a Full-Scale Proprotor on the Tiltrotor Test Rig," *VFS Aeromechanics for Advanced Vertical Flight Technical Meeting*, Vertical Flight Soc., Fairfax, VA, Jan. 2020, pp. 1–15.
[18] Kreshock, A. R., Thornburgh, R. P., Wilbur, M. L., Kang, H., Piatak, D. J., and Sekula, M., "Initial Whirl-Flutter Characterization of the TiltRotor Aeroelastic Stability Testbed," *Vertical Flight Society 79th Annual Forum*, Vertical Flight Soc., Fairfax, VA, May 2023, pp. 1–18. https://doi.org/10.4050/F-0079-2023-18037
[19] Thornburgh, R. P., Kreshock, A. R., Kang, H., Ivanco, T. G., Sekula, M. K., and McHugh, G. R., "An Experimental Parametric Study on the Whirl-Flutter Stability of Tiltrotors," *Vertical Flight Society 81st Annual Forum*, Vertical Flight Soc., Fairfax, VA, May 2025, pp. 1–12. https://doi.org/10.4050/F-0081-2025-205
[20] Kreshock, A. R., Thornburgh, R., and Wilbur, M., "Overview of the TiltRotor Aeroelastic Stability Testbed," *AIAA SCITECH 2022 Forum*, AIAA Paper 2022-0566, 2022. https://doi.org/10.2514/6.2022-0566
[21] Montaño-Oliveros, J., Fonte, F., van't Hoff, S., and Timmerman, B., "Whirl Flutter Analysis of a Tiltrotor Semi-Span Wind Tunnel Model for Test Results Correlation," *49th European Rotorcraft Forum*, DGLR-Bericht, Sept. 2023, pp. 1–17.
[22] van't Hoff, S., van Vilsteren, J., Cocco, A., and Masarati, P., "Design of a Tiltrotor Semi-Span Wind Tunnel Model for Whirl Flutter Investigations," *AIAA SCITECH 2023 Forum*, AIAA Paper 2023-1306, 2023. https://doi.org/10.2514/6.2023-1306
[23] Gul, S., and Datta, A., "Design Analysis for a Mach-Scaled Hingeless Hub for the Maryland Tiltrotor Rig," *8th Asian/Australian Rotorcraft Forum*, Vertical Flight Soc., Fairfax, VA, Oct.–Nov. 2019, pp. 1–9.
[24] Gul, S., and Yeo, H., "Correlation of High-Speed Tiltrotor Stability Predictions with Test Data and Parametric Study," *Journal of Aircraft*, Vol. 61, No. 4, 2024, pp. 1283–1292. https://doi.org/10.2514/1.C037807
[25] Sutherland, J., and Datta, A., "Fabrication, Testing, and 3D Comprehensive Analysis of Swept-Tip Tiltrotor Blades," *Journal of the American Helicopter Society*, Vol. 68, No. 1, Jan. 2023, pp. 1–17. https://doi.org/10.4050/JAHS.68.012002
[26] Acree, C., "Effects of V-22 Blade Modifications on Whirl Flutter and Loads," *Journal of the American Helicopter Society*, Vol. 50, No. 3, July 2005, pp. 269–278. https://doi.org/10.4050/1.3092863
[27] Srinivas, V., Chopra, I., and Nixon, M. W., "Aeroelastic Analysis of Advanced Geometry Tiltrotor Aircraft," *Journal of the American Helicopter Society*, Vol. 43, No. 3, July 1998, pp. 212–221. https://doi.org/10.4050/JAHS.43.212
[28] Rosenstein, H., and Clark, R., "Aerodynamic Development of the V-22 Tilt Rotor," *Aircraft Systems, Design and Technology Meeting*, AIAA Paper 1986-2678, 1986. https://doi.org/10.2514/6.1986-2678
[29] Hammond, C. E., and Doggett, R. V. Jr, "Determination of Subcritical Damping by Moving-Block/Randomdec Applications," *NASA Symposium on Flutter Testing Techniques*, NASA SP 415, Oct. 1975, pp. 59–76.
[30] Bousman, W., and Winkler, D., "Application on the Moving-Block Analysis," *Dynamics Specialists Conference*, AIAA Paper 1981-0653, 1981. https://doi.org/10.2514/6.1981-653
[31] Hauer, J. F., Demeure, C. J., and Scarf, L. L., "Initial Results in Prony Analysis of Power System Response Signals," *IEEE Transactions on Power Systems*, Vol. 5, No. 1, Feb. 1990, pp. 80–89. https://doi.org/10.1109/59.49090
[32] Akinwale, A., and Datta, A., "High Speed Whirl Flutter Tests of the Maryland Tiltrotor Rig," *Vertical Flight Society 79th Annual Forum*, Vertical Flight Soc., Fairfax, VA, May 2023, pp. 1–17. https://doi.org/10.4050/F-0079-2023-18035
[33] Gul, S., and Datta, A., "Development of an Aeromechanics Solver for Loads and Stability of Hingeless Tiltrotors," *Journal of Aircraft*, Vol. 60, No. 1, Jan. 2023, pp. 143–159. https://doi.org/10.2514/1.C036944

I. Chopra
Associate Editor